Zero field optical study of phosphorus magnetic resonance in enriched silicon

by

Kevin Morse

B.Sc., Simon Fraser University, 2013

Thesis Submitted in Partial Fulfillment
of the Requirements for the Degree of
Master of Science

in the
Department of Physics
Faculty of Science

ⓒ Kevin Morse 2016
SIMON FRASER UNIVERSITY
Summer 2016

Approval

Name:	Kevin Morse
Degree:	Master of Science (Physics)
Title:	*Zero field optical study of phosphorus magnetic resonance in enriched silicon*
Examining Committee:	**Dr. Malcolm Kennett** (chair)
	Assistant Professor

Dr. Michael Thewalt
Senior Supervisor
Professor

_____

Dr. David Broun
Supervisor
Associate Professor

_____

Dr. Stephanie Simmons
Internal Examiner
Assistant Professor

_____

Date Defended: August 11, 2016

Abstract

Silicon-based qubits are one of the most promising technologies for the construction of a quantum computer. The nuclear spins of phosphorus donors in enriched silicon have among the longest coherence times of any solid-state system. In this thesis, I examine the phosphorus in silicon system in the regime of "zero" magnetic field. Laser spectroscopy and magnetic resonance are used to characterize the phosphorus in silicon system in this environment. I show the system can be hyperpolarized and has $\sim 10\,\mathrm{s}$ coherence times. Additionally, the methods and apparatus developed for this study prove useful for the study of other similar but more exotic systems.

Keywords: magnetic resonance; quantum information;

Acknowledgements

A large number of people deserve recognition for helping me complete this thesis and my degree.

First and foremost, I must thank my Senior Supervisor, Mike Thewalt, for his help both in the lab and while writing this thesis as well as for the tremendous amount of knowledge he has shared with me over the past couple years. I would also like to thank Dave Broun who has been an invaluable resource whenever I am working on a new experiment.

I must also thank the other graduate students (current and past) in the Thewalt group: Rohan Abraham, Phil Dluhy, Jeff Salvail, and Kamyar Saeedi-Ilkhchy as well as Julian Huber who visited from Austria for a semester.

The many skilled technicians both in and out of the department deserve mention for all the assistance that they have provided with this and other projects. Ken Van Wieren, Jim Shoults, and Howard Proulx from the Machine Shop helped me make countless adapting plates, brackets, and boxes. Ray Holland, Pawel Kowalski, Anthony Slater, and John van der Est in the Electronics Shop put up with my back and forth trips for various electronic components. Bryan Gormann and Ken Myrtle in the department who never hesitated to drop whatever they were doing when I was stuck with a project.

Finally, I must thank my friends and family for always helping me stay focused and positive when I was struggling with courses or sick of writing. Without you, I would probably still be writing.

Table of contents

List of tables

List of figures

Chapter 1

Introduction

Silicon is one of the most important elements to modern civilization. Its use as the foundation material for integrated circuits, the building block of modern computers, means practically all electronic technology in use today depends on it. Given its tremendous importance it's no surprise that silicon has been studied extensively over the last fifty years. Today silicon is one of the most well researched and understood materials in the world.

Much of this research effort has been spent studying impurities and purification. Before silicon can be used in the fabrication of integrated circuits it must first be purified. This is necessary as the presence of impurities in silicon can have significant effects on its electrical properties. Once purified, impurities are added back into the silicon in a controlled process called doping. It is these dopants, called donors or acceptors depending on whether they "donate" or "accept" an electron that enable silicon to act as a semiconductor.

Phosphorus, a common donor in semiconductor manufacturing, is also the basis of a proposal to construct a silicon based quantum computer [1]. In this proposal, the author, Bruce Kane of UNSW, envisions storing information using the nuclear spin (up or down) of phosphorus donors in silicon. Manipulating the information by changing the spin could be done using electric field. Measurement of the nuclear spins and the information it contains could be performed using electrical current. One of the many requirements of this proposal is that the silicon, except for the phosphorus donors, should contain only nuclei with zero spin. This is needed to prevent information stored in the phosphorus nuclear spin from being affected by the nuclear spins of the surrounding silicon lattice.

1.1   Avogadro project

Several years after this proposal, a completely separate international project was started with the aim of redefining the kilogram. This redefinition would be in terms of the atomic mass of either silicon or carbon and the Avogadro constant, $N_A \approx 6.022 \times 10^{23}$ atoms/mol. Redefinition of the kilogram is important as it is the only SI unit not defined by a constant

of nature. Instead, the kilogram is defined by the mass of a small platinum-iridium cylinder called the International Prototype Kilogram (IPK, also known as "Le Grand K"). The problem is that the IPK is changing in mass over time when compared to copies of it that are kept in labs around the world.

A changing kilogram is problematic for many experiments which rely on very accurate measurements of mass for their results. Ultimately it was decided to work with silicon for this project, likely due to the vast amount of knowledge that exists on purifying silicon.

In order for this redefinition to take place, nearly perfect spheres of silicon were manufactured. By precisely measuring volume V, lattice spacing a, and mass m it is possible to determine N_A provided the atomic mass M is known [2].

$$N_A = \frac{8MV}{a^3 m} \tag{1.1}$$

Since natural silicon is composed of three stable isotopes (silicon-28, silicon-29, and silicon-30), it is impossible to know the atomic mass of natural silicon accurately enough to redefine the kilogram. The solution is to use isotopically enriched silicon-28 (^{28}Si). This isotope was chosen as it is the most abundant (92% of natural silicon) and therefore the easiest to enrich. It also happens to have a nuclear spin of zero which makes it useful as far as the Kane proposal goes.

In order to measure the purity of the ^{28}Si enriched for the Avogadro project, high resolution spectroscopy measurements were carried out by the Thewalt group at SFU. During these measurements it was determined that the transition line-widths of various impurities still present became very narrow. The line-widths were so narrow that the transitions associated with individual spin states could be resolved [3]. Further work by the Thewalt group established that both the nuclear and electron states could be polarized [4].

Given the above, it makes sense to continue the study of phosphorus in silicon as a candidate material for the next generation of computers, the quantum computer.

1.2 Quantum computing

Whereas the current generation of computers, hereafter referred to as classical computers, make use of bits to store information in the form of zeros and ones, quantum computing makes use of quantum bits which can store information not only as a zero or a one but as "superposition" of both zero and one at the same time. Although qubits can store multiple values, when measured they will only yield a single value. The value obtained is dependent on a probability associated with each value. This probability can be varied by performing operations on the qubit.

Another unique property of quantum systems is entanglement. This is when the values of two or more qubits become correlated even when separated by great distances. The pair

or group of qubits cannot be described independently but instead must be described as a complete system.

Together these properties enable both an exponential speedup of certain algorithms and the ability to simulate quantum systems that cannot be efficiently simulated with classical computers. The ability to simulate these systems could enable new breakthroughs in electronics, medicine, and materials science. There is potential to make communication more secure while at the same time the speedup of some algorithms could defeat many existing encryption technologies.

In addition to the other properties, quantum systems also exhibit something called coherence. Coherence is the length of time that a 'superposition' state can survive. The coherence time of a qubit system is very important to quantum computation. Even a system which could be easily initialized to any state would be of little use for quantum computation if the state didn't survive long enough to perform an operation or measurement.

The coherence time of a qubit system also has an impact on the scalability of a given architecture due to the necessity of error-correction in quantum computation. Error-correction is a technique that is employed to limit the effects of decoherence on the accuracy of a calculation. Since error-correction works by spreading information across several qubits, the number of qubits needed for accurate computation is related to how much error-correction is needed and therefore the coherence time of the qubit.

1.3 Donors in silicon

In 2013, the Thewalt group performed coherence measurements of the phosphorus nuclear spin in enriched silicon resulting in world record coherence times of 39 minutes at room temperature and over 3 hours at liquid helium temperature [5]. This result was groundbreaking when compared to coherence times of other systems such as nitrogen-vacancy (NV) centers in diamond which, at the time, had coherence times of $\sim 2\,\mathrm{s}$ [6] and helped donors in silicon become one of the most widely used systems for quantum information research. [7, 8, 9]

One similarity between almost all of the previous research done on donors in silicon is the need for relatively high magnetic fields. The 39 minute result required the use of a large water cooled electromagnet (roughly ten times the strength of a typical refrigerator magnet and weighing tens of kilograms) and most research since then has made use of the far higher fields produced by superconducting magnets. In addition to the added size and weight, superconducting magnets also require cryogenic temperatures and introduce a considerable heat load into the system.

Furthermore, the radio frequencies required to work with a donor qubit at low magnetic field quickly increase with field well into the microwave regime (tens of GHz). Dealing with microwaves not only requires the use of more complicated (and costly) electronics but also

requires resonators to deliver the microwaves to the qubit. Transmission losses are also higher at these frequencies so amplification is often required.

Conversely, operating at zero- or low-field reduces complexity significantly, no magnets are required and the frequencies are much more manageable (~ 100 MHz for phosphorus and < 10 GHz for all other donors [10]) however it also introduces some challenges. Traditional nuclear magnetic resonance (NMR) or electrically detected magnetic resonance (EDMR) [11] requires a quantization axis but at zero-field there isn't one. That the separation between the different states is very small is advantageous in that it keeps the required frequencies low but it also makes resolving the separate states much more difficult.

Thankfully, both of these hurdles can be overcome using optical polarization and read-out, which requires no quantization axis and is able to resolve very narrow transitions. Using these optical techniques, pioneered by the Thewalt Lab, in conjunction with standard magnetic resonance techniques developed decades ago, allows us to study phosphorus in silicon at zero-field.

This thesis will begin with an explanation of the theory that enables these techniques to work before outlining the methods and apparatus employed in this study. I will then present results specific to phosphorus in ^{28}Si including optical and magnetic resonance spectra as well as data from pulsed magnetic resonance experiments. Although the coherence times at zero-field are shorter than the coherence times at field they are still longer than those of competing technologies and should be sufficiently long for use in quantum computation. Finally, I will conclude with a summary of the results and a brief outline of how the methods and apparatus used in this work are being reused to study selenium in silicon.

Chapter 2

Background and theory

2.1 Donor impurities in silicon

The quantum system used for this work is phosphorus in isotopically enriched silicon. Phosphorus is a group-V element while silicon is a group-IV element. The lattice of silicon is a face-centred cubic with a basis of two atoms per lattice point. This structure is also known as the diamond structure. Since silicon has four valence electrons, all are used in the covalent bonding.

When a phosphorus atom is introduced into a silicon crystal it takes the place of a silicon atom. Since phosphorus has five valence electrons, four are used for covalent bonding and the left over electron is called the donor electron.

Since 14 of the bound electrons and 14 of the protons in the phosphorus nucleus are indistinguishable from the 14 electrons and 14 protons of the ^{28}Si, the system can be thought of as a lattice with no spin that has a single proton and electron, bound to it by Coulomb interaction, at the site of each phosphorus impurity. This system is then analogous to a hydrogen atom in a vacuum [12]. For this study only the ground electronic state of the neutral phosphorus donor is relevant, with a binding energy of 45 meV [13].

2.1.1 The hyperfine Hamiltonian

Considering only the contact hyperfine interaction between the donor electron and nuclear spin[1], the spin Hamiltonian for the neutral donor (D^0) ground state in an applied magnetic field $B_0\hat{z}$ can be written,

$$\mathcal{H}_{D^0} = \gamma_S B_0 S_z - \gamma_I B_0 I_z + A\vec{S}\cdot\vec{I}, \tag{2.1}$$

---

[1]We neglect spin-orbit coupling as it is very small in silicon. [14, 15]

where A is the hyperfine constant and $\vec{S}$ and $\vec{I}$ are the spin operators of the electron and nucleus respectively. The constants γ_S and γ_I are defined as follows,

$$\gamma_S = \frac{g_e \mu_B}{h}, \quad \gamma_I = \frac{g_n \mu_N}{h},$$

where g_e is the electron g-factor, g_n the nuclear g-factor, μ_B the Bohr magneton, μ_N the nuclear magneton, and h the Planck constant. We divide by h in order to work in frequency units where $A = 117.53\,\mathrm{MHz}$, $\gamma_S = 27.972\,\mathrm{MHz/mT}$ and $\gamma_I = 17.251\,\mathrm{kHz/mT}$. The eigenvalues of (2.1) are given by the Breit-Rabi formula:

$$\frac{E\left(F = I \pm 1/2, M\right)}{\frac{1}{2}A\left(2I + 1\right)} = \pm \frac{1}{2}\sqrt{x^2 + \frac{4M}{2I+1}x + 1} - \frac{Mx}{\frac{\gamma_S}{\gamma_I} + 1} - \frac{1}{2(2I+1)}, \tag{2.2}$$

where F is the total atomic angular momentum $(S+I)$ and ranges from $I - 1/2$ to $I + 1/2$, M is the projection of the total angular momentum $(m_S + m_I)$ and ranges from $-F$ to $+F$, and I is the nuclear spin. The dimensionless field x is defined as follows,

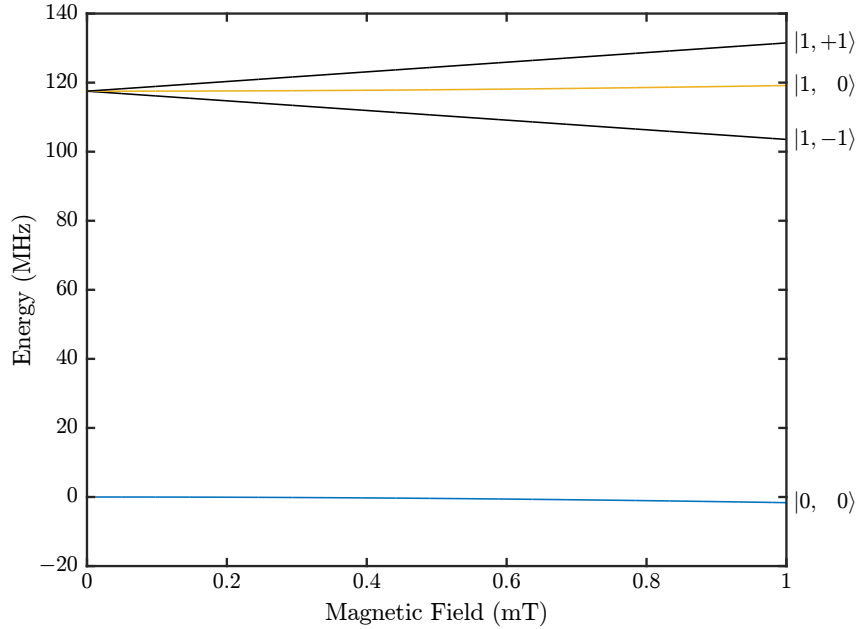$$x = \frac{\gamma_S + \gamma_I}{\frac{1}{2}A\left(2I + 1\right)}B_0.$$

Figure 2.1: Energy levels of the ^{31}P Zeeman states relative to the $|F = 0, M = 0\rangle$ state.

The eigenvalues for ^{31}P are shown in Fig. 2.1. Ignoring the second term of (2.2) since $\gamma_S \gg \gamma_I$, the eigenvalue equations for ^{31}P are as follows:

$$E\left(F = 1, M = +1\right) = A\left(+\frac{1}{2}(1 + x) - \frac{1}{4}\right) \tag{2.3}$$

$$E\left(F = 1, M = 0\right) = A\left(+\frac{1}{2}\sqrt{1 + x^2} - \frac{1}{4}\right) \tag{2.4}$$

$$E\left(F = 1, M = -1\right) = A\left(+\frac{1}{2}(1 - x) - \frac{1}{4}\right) \tag{2.5}$$

$$E\left(F = 0, M = 0\right) = A\left(-\frac{1}{2}\sqrt{1 + x^2} - \frac{1}{4}\right) \tag{2.6}$$

For $B_0 = 0$, these reduce to two eigenvalues, with total spin $F = 1$ and $F = 0$, separated by A, with the $F = 0$ state lower in energy than the $F = 1$ state. For $B_0 > 0$, these two states split into $2F + 1$ Zeeman components, giving three states with $F = 1$ and one state with $F = 0$. A standard way of labelling these states is from $|1\rangle$ to $|4\rangle$ in order of increasing energy (remembering that at very high B_0, there is a crossing of the $|3\rangle$ and $|4\rangle$ states). However, in this thesis they will be labelled $|F, M\rangle$. This labelling scheme results in the four states being labelled $|0, 0\rangle$, $|1, -1\rangle$, $|1, 0\rangle$, and $|1, +1\rangle$.

By applying electromagnetic radiation of a specific frequency to the neutral donor we can facilitate the transition from the $F = 0$ branch to one of the $F = 1$ states. The three different transition frequencies are shown as a function of field in Fig. 2.2. At the fields used in this thesis ($B < 20\,\mu$T) the $0 \to 0$ transition frequency is essentially constant while the $0 \to \pm 1$ transitions vary approximately linearly with B_0. This is shown in Fig. 2.3 a plot of the derivatives of the transition frequencies as a function of magnetic field.

Looking at the derivatives we see that $\partial f_{0 \to 0}/\partial B = 0$ at $B = 0$. This means zero field is a so called "clock transition" (CT) for the $0 \to 0$ transition. Clock transitions are important, since they remove the dependence of the transition frequency on B_0. [16, 17] Although we are operating at extremely low fields there are certainly still fluctuations of the magnetic field as well as field inhomogeneity. Operating at a clock transition minimizes the effect of these sources of decoherence.

2.1.2 Donor bound excitons

A donor bound exciton (D^{0}X) is an electron-hole pair bound to a neutral donor through dipole-dipole coupling. The exciton electron and the donor electron form a spin singlet which leaves the exciton hole and the donor nucleus free to take any allowed spin. Since the hole is spin 3/2 and the nucleus is spin 1/2 the donor bound exciton has eight spin eigenstates. However, since there is no hyperfine coupling the nuclear spin states in the bound exciton have negligible energy splitting and therefore cannot be optically detected.

Fig. 2.4 shows how shining photons of a specific energy onto the sample can create D^{0}X resonantly. The D^{0}X have relatively short lifetimes and decay through Auger ionization
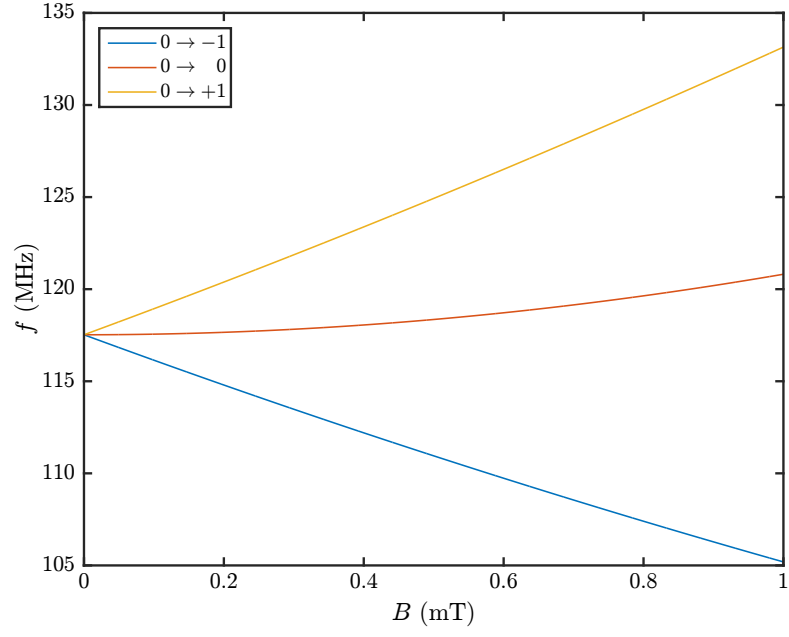
Figure 2.2: Frequencies of the allowed transitions of ^{31}P in silicon at low field.
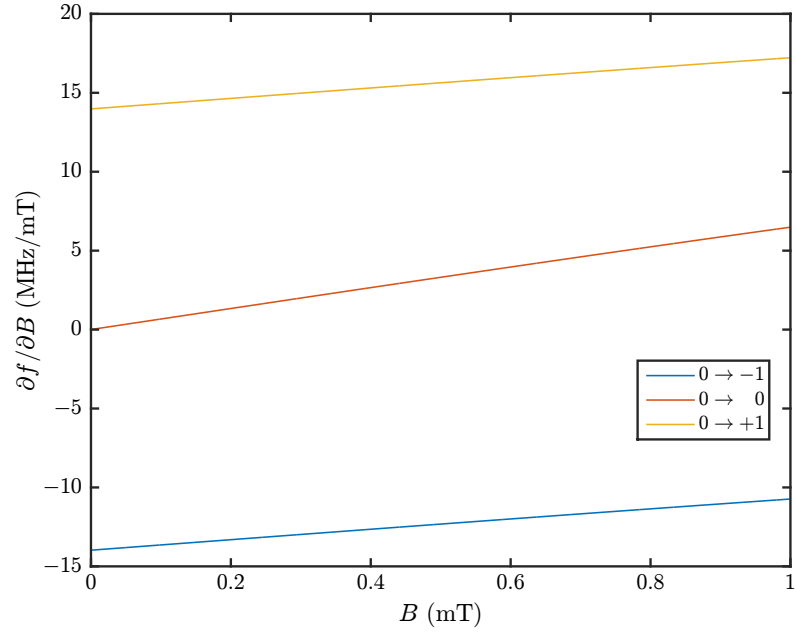

Figure 2.3: Derivatives of the transition frequencies of ^{31}P in silicon at low field.

[18]. Although the field of the diagram is much higher than the field used for my results, the same process occurs. One of the electrons recombines with the hole and the energy of this recombination ionizes the remaining electron. This ionized electron can be detected by measuring the impedance of the sample since more free electrons in the conduction band reduce the impedance. The optically-induced conductivity is thus proportional to the population of donors in the nuclear state being probed by the laser.
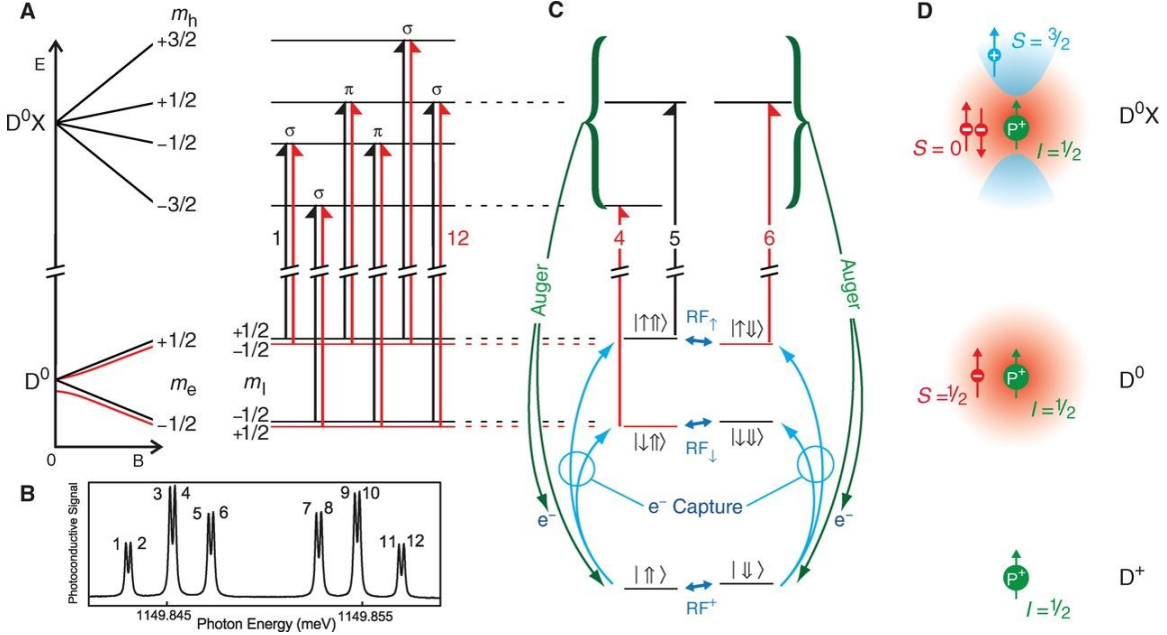

Figure 2.4: **A:** Zeeman splittings of the D^0 and D^0X states along with the dipole-allowed optical transitions from $B = 0\,\text{mT}$ to $B = 84.5\,\text{mT}$. **B:** Photoconductive readout spectrum. **C:** The specific optical transitions (lines 4, 5, and 6) and nuclear magnetic resonance transitions ($RF_\uparrow$, $RF_\downarrow$, and RF^+) used here to hyperpolarize, manipulate, and read out the nuclear spins. The magnitude of the D^+ Zeeman splitting (RF^+) has been exaggerated to show the ordering of the D^+ states, and the small nuclear Zeeman energy is ignored for the D^0X states. **D:** Sketches of the spins and charge densities of D^0X, D^0, and D^+. [5]

2.2   Magnetic resonance

Implementing a quantum computer will require not only quantum bits but quantum logic gates. These logic gates will manipulate the quantum bits to perform calculations. Since the qubits in this case are the spins of the donor electron and nucleus, we can think of their states as points on a Bloch sphere. To manipulate the states is to apply rotations to the spins.

Since the spins have magnetic dipole moments, we use pulsed magnetic resonance to apply the rotations. In the low B_0 regime studied here, the electron and nuclear spins are coupled and the transitions are not purely EPR- or NMR-like. Magnetic resonance involves

9

a static field, B_0, and a time varying field B_1. In the absence of B_1 we expect the spins to align along B_0. From there we apply RF at one of the transition frequencies using the B_1 coil. These pulses rotate the spins away from the B_0 axis with the magnitude of the rotation being dependent on the incident power and duration of the pulse.

There were three types of pulse sequences used in this thesis: Rabi, Ramsey, and Hahn. Each has a different purpose as will be explained below.
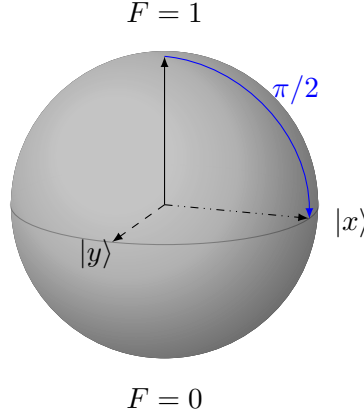
Figure 2.5: A Bloch sphere diagram showing a $\pi/2$-pulse rotating a spin from an $F = 1$ state into the $\hat{x}$-$\hat{y}$ plane.

2.2.1 Rabi oscillation
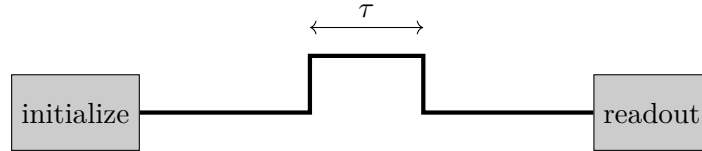
Figure 2.6: Rabi pulse sequence

The Rabi oscillation is typically the first pulsed measurement used when conducting magnetic resonance studies. For our experiment, it consists of a single RF pulse followed by a readout sequence using one or more lasers. The duration of the pulse is increased after each cycle. For the measurements in this thesis, the readout of one cycle served as the initialization sequence for the next cycle.

As seen in Fig. 2.5, the magnetic pulse rotates the spin by an angle proportional to the incident power and duration of the pulse. After each pulse the readout provides a measure of the polarization projected onto the $\hat{z}$ axis. As the duration is increased the polarization should theoretically oscillate like a cosine between $\pm 100\%$ but in practice the oscillations are damped.

Looking at the period of oscillation allows us to determine the pulse lengths required to perform a $\pi/2$- or π-rotation. This information is required for the Ramsey and Hahn measurements.

Since the actual B_1 magnitude depends on output power of the source, coil matching, and any losses between the source and the coil, it tends to vary. For this reason a Rabi measurement is typically performed at the beginning of each set of measurements and after any change to the apparatus or source power.

2.2.2 Ramsey fringes

The next measurement performed is the Ramsey fringe experiment. This measurement provides information on the T_2^* time and the frequency offset of the applied pulse relative to the actual transition frequency. The T_2^* is the relaxation time constant due to magnetic field inhomogeneity and roughly matches the $1/e$ time of the free induction decay in a normal magnetic resonance experiment.

Because we are performing our measurements on many spins in a bulk crystal and the B_1 field is not perfectly uniform, each spin experiences a slightly different field and therefore acquires a slightly different phase. As the free-evolution time increases, the difference in phase between spins increases, and the envelope of the Ramsey interference fringes decays exponentially. The time constant of this envelope is called the T_2^*. This parameter provides an estimate of the duration with which coherence can be maintained under free evolution.
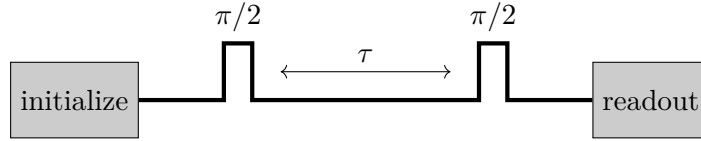
Figure 2.7: Ramsey pulse sequence

This Ramsey measurement consists of two $\pi/2$-pulses separated by a delay τ as shown in Fig. 2.7. The first pulse rotates the spins $\sim 90°$ from $\hat{z}$, the spins then precess around $\hat{z}$ for the free-evolution time τ before being rotated back into $\hat{z}$ for readout. If the precession frequency ω of the spins is not exactly equal to the frequency of the applied pulse ω_{RF} then the spins will acquire a phase during the free-evolution time τ. This phase interference as a function of time τ will be visible in the form of oscillations at a frequency equal to the difference between ω and ω_{RF}.

2.2.3 Hahn (spin) echo

The final type of pulse sequence used in our magnetic resonance experiments is the spin echo also known as the Hahn echo after Dr. Erwin Hahn who discovered it in 1950. The Hahn echo enables measurement of the T_2 coherence time. As mentioned above, as the free-

Figure 2.8: Hahn pulse sequence

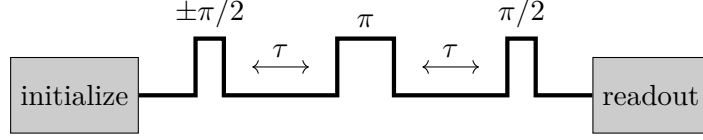evolution time increases so to does the difference in phase between the spins. By flipping the spins by $180°$ using a π-pulse after a free evolution time τ, the spins start to rephase, and rephase completely after a second time τ. In this way, the inhomogeneous effects which caused the dephasing will be cancelled out and the observed decay due to slow fluctuations in the magnetic environment can be measured.

The pulse sequence used for the Hahn echo can be seen in Fig. 2.8. As with the Ramsey measurement, $\pi/2$-pulses are used to rotate the spins away from $\hat{z}$ so they can evolve and then back to $\hat{z}$ for measurement. The only addition is the π inversion pulse in the middle of the sequence. Like the Ramsey measurement the parameter varied is the delay between the pulses. In this case the parameter is often labelled 2τ since there are two delays.

For the measurements made in this thesis, a small modification to the standard Hahn echo sequence, termed phase cycling, was used. With phase cycling, the first $\pi/2$-pulse is phase shifted by $180°$ every other repetition. The amplitude of the $180°$ shifted repetition is then subtracted from the amplitude of the unshifted repetition to give an amplitude with a true zero. This works because at long times, when there is no coherence left the amplitude measured from the shifted and non-shifted repetitions will both be the same.

Chapter 3

Experimental methods

3.1   Sample

The sample studied for this research is a small $5.0 \times 4.7 \times 1.7$ mm piece cut from a slice of the Avogadro crystal (Si28-10Pr11.02.2). This crystal was grown by the Leibniz Institute for Crystal Growth (Leibniz-Institut für Kristallzüchtung) as part of the Avogadro project and was enriched to 99.995% ^{28}Si [19]. After being cut to size using an inner-diameter saw, the sample was etched in a $10 : 1$ mixture of $HNO_3 : HF$ to remove surface damage. This step is important as surface damage causes strain which leads to splitting of the spectral lines.

Impurity concentrations were determined using photoluminescence spectroscopy [20] to be $\sim 5 \times 10^{11}\,\mathrm{cm}^{-3}$ phosphorus and $5 \times 10^{13}\,\mathrm{cm}^{-3}$ boron. The sample was also found to contain $< 10^{13}$ cm^{-3} oxygen and $< 10^{14}$ cm^{-3} carbon.
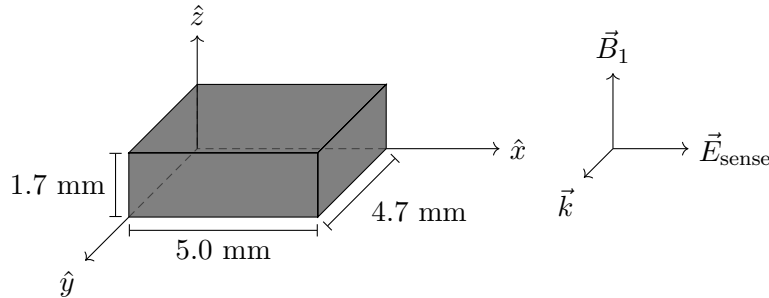

Figure 3.1: Diagram of the sample showing dimensions and orientation. The electrodes used for capacitive readout were parallel to the $\hat{y}$-$\hat{z}$ plane, generating a field $\vec{E}_{\mathrm{sense}}$ across the sample, the B_1 coil was wound around the $\hat{z}$-axis, and the laser light, $\vec{k}$, was incident along the $\hat{y}$-axis.

3.2 Experimental setup

3.2.1 Zero field sample holder

The sample was mounted in a 3D printed sample holder made out of "high performance composite material" and a piece of silica. This was designed to hold the sample in a strain-free manner, prevent it from falling out, and locate it between two pieces of copper foil used for the capacitive conductivity readout. The sample holder slots into the center of a plastic Helmholtz coil form on the end of a fibreglass rod. The Helmholtz coil (3.5 turns $\sim 26\,\mathrm{mm}$ in diameter) was tuned to approximately $117\,\mathrm{MHz}$ and impedance matched to the $50\,\Omega$ transmission line using a $2\,\mathrm{pF}$ series capacitor.

This assembly was inserted into a non-magnetic stainless steel immersion dewar made by Janis Research. The dewar used was specifically chosen as it had never been placed in a magnetic field. This was important as preliminary testing showed remnant fields existed in other similar dewars that had been previously used in high magnetic fields. We suspect the remnant field is trapped in the ferromagnetic inclusions introduced during welding.

The tail of the dewar was shielded by wrapping several layers of high permeability 80% nickel alloy foil around it. For further shielding the entire bottom section of the cryostat (including the tail and nickel alloy foil) had two layers of GIRON, a woven magnetic shielding material, wrapped around it. After the shielding was added the field was measured to be around $4\,\mathrm{\mu T}$. In order to get to even lower fields, three coil pairs were wound around the tail of the dewar but inside the shielding along the $\hat{x}$, $\hat{y}$, and $\hat{z}$ axes. The tail had a fused silica window and a single small hole was cut into each layer of shielding to allow the laser light to reach the sample.

3.2.2 Laser configuration

A number of different lasers were used in this thesis, two of the most important being a Koheras ADJUSTIK Y10 fibre laser and a Toptica DL 100 tunable diode laser. As the frequency of a laser can depend on a number of different conditions such as current, temperature, or the position of an internal grating or mirror it is necessary to have a way of accurately measuring and controlling it.

To this end, the Thewalt lab employs a temperature controlled quartz cavity which both the Koheras fibre laser and Toptica diode laser are shone into as well as a frequency stabilized HeNe laser. The position of the HeNe interference fringe is used to fix the temperature of the cavity while the interference fringes of the fibre and diode lasers are used to provide feedback to the respective laser controllers as follows.

The Koheras laser is locked to the cavity using a proportional-integral (PI) controller connected to an internal piezoelectric actuator and an additional slower integrator connected to the temperature controller of the laser. The internal piezoelectric actuator is responsible

for making rapid small adjustments to the output wavelength while the temperature of the laser is used to gradually sweep the wavelength over the course of a laser frequency scan.

The Toptica laser is also locked to the cavity using a PI controller, which I constructed, to adjust the current supplied to the laser diode. Changing the diode current allows for rapid small adjustments to the output wavelength similar to the way the piezoelectric actuator can affect the output of the fibre laser.

Both lasers are scanned by using a mirror galvanometer to shift the position of the interference fringe. As the galvanometer shifts the position of the interference fringes, the PI controller adjusts the wavelength of the laser to minimize the error signal. In this way, the lasers are both frequency stabilized and scanned using the same feedback system. [21]

Both lasers are connected to ytterbium-doped fibre amplifiers as well as an optical switch which allows either laser wavelength to be measured by a Bristol 621 wavelength meter. Measuring the wavelength is necessary because the locking and scanning system has no way of knowing which interference fringe (and therefore what exact wavelength) it has locked to when first turned on.

Finally the outputs of the laser amplifiers are collimated into free space, passed through shutters, and aligned to the same beam path. They are guided to the sample using gold first surface mirrors to minimize signal loss. A chopper wheel is sometimes used in the optical path of one or both of the lasers to modulate the laser when using synchronous detection.

Lastly we used a 200 mW CrystaLaser 1047 nm diode pumped laser. At 1047 nm $\approx$ 1.18 eV, its energy is just above the silicon band gap ($\sim$1.17 eV at liquid helium temperature) and so we call it the "above-gap" laser. Above-gap excitation is used to produce free carriers within the sample which photoneutralize the ionized donors and acceptors. This reduces random electric fields within the sample, sharpening lines and increasing coherence times. Too much above-gap light effectively "shorts out" the sample, so this beam was attenuated using neutral-density (ND) filters.

3.2.3 Photoconductive readout

In the Auger decay of a D^0X, energy from the recombination of the electron-hole pair ionizes the neutral donor, D^0, leaving behind an ionized donor, D^+, and a free electron. Photoconductivity from the free electrons can be detected by measuring the impedance of the sample using non-contact capacitive coupling. This technique is called photoconductive (PC) readout.

Figure 3.2 illustrates the setup used to measure the sample impedance. The setup uses lock-in detection of an AC signal through an impedance, the sample. The signal is a sine-wave with frequency around 117 kHz and amplitude of $\sim$20 V_{pp}. As mentioned in Section 3.2.1, the sample is mounted between two sheets of copper, which serve as the plates of a parallel plate capacitor, generating a field $\vec{E}_{sense}$ across the sample. In parallel with the sample is a phase shifting (PM) and amplitude attenuating (AM) circuit in series with a
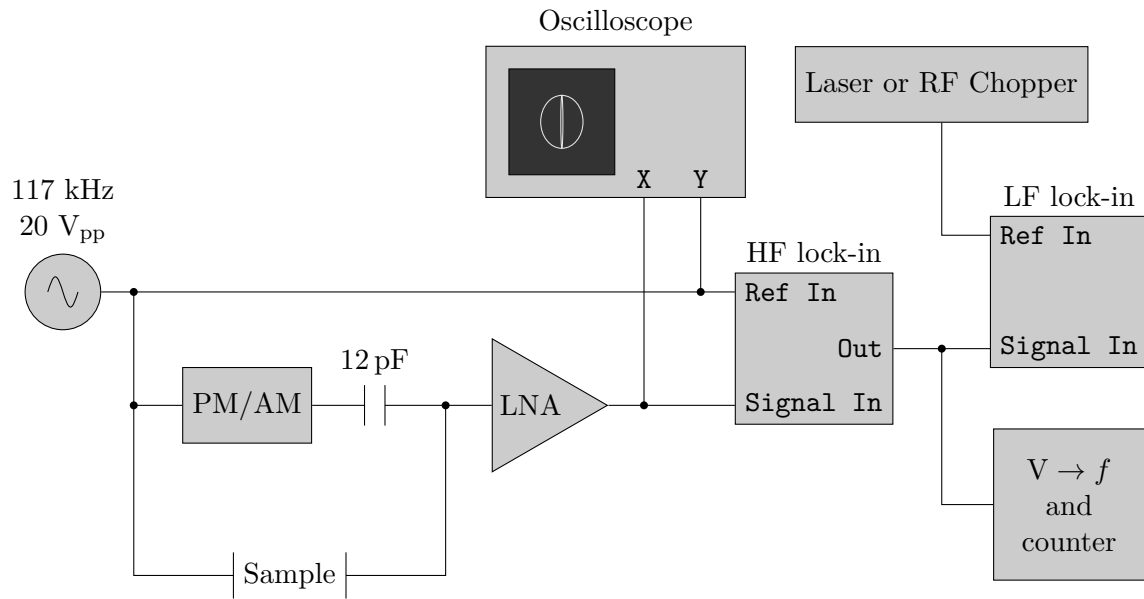
Figure 3.2: A schematic showing the components of the PC readout. A function generator is connected to the lock-in amplifier reference, nulling circuitry (PM/AM), and one of the copper plates in loose contact with the sample. The other copper plate and the output of the nulling circuitry are connected to a low noise preamplifier. Using the nulling circuitry and the oscilloscope, the signal into the HF lock-in can be minimized when the laser excitation is blocked. The HF lock-in is connected to either a LF lock-in or a voltage-to-frequency converter depending on the measurement being performed.

12 pF capacitor[1]. This allows the signal into the low noise preamplifier (LNA) to be nulled (minimized) for a specific experimental condition, e.g. a sample in the dark or a sample in steady-state under illumination by the read-out laser. An oscilloscope in XY mode assists with the setting of this null condition.

The output of this lock-in, hereinafter referred to as the high frequency (HF) lock-in, is measured in a number of different ways depending on the type of measurement being performed.

3.3 Measurement techniques

3.3.1 Optical scans

In order to capture the optical spectra of phosphorus in silicon, the fibre laser is scanned across the frequency range of interest while the output beam is chopped at 20 Hz to 200 Hz[2]. The signal due to the chopped laser is extracted from the photoconductive signal output by the HF lock-in using a second lock-in amplifier, the low frequency (LF) lock-in, with the chopper frequency as its reference. The LF lock-in is connected to a computer running LabVIEW. A single LabVIEW VI is used to acquire the laser signal as well as calibrate, move, and scan the laser.

To observe hyperpolarization caused by optically pumping a transition, the diode laser can also be used in addition to the scanning fibre laser. In this case only the scanning laser is chopped while the diode laser is tuned to a single line.

Continuous above-gap excitation from the 1047 nm laser is used to enhance the SNR of the spectra. The weak above-gap radiation generates electrons and holes which photoneutralize the D^+ and A^-. This increases D^0X creation resulting in more signal and reduces Stark broadening causes by the electric fields of the fixed ionized impurities.

3.3.2 Magnetic resonance scans

RF scans of the ^{31}P magnetic resonance transitions are performed in a similar manner but with two key differences: the RF is scanned and chopped while the laser remains on and at a constant frequency the entire time. The RF is switched on and off using 13 Hz TTL pulses to control a high isolation RF switch[3] connected to the output of the RF source. Such a switch is typically used for transmitter-receiver isolation but in this case the second input is connected to a 50 Ω load. The signal from the RF is extracted using the same LF lock-in connected to a computer as above.

---

[1]Either a 1.2 pF or 12 pF capacitor is used depending on which requires the least adjustment from the phase shifting and amplitude attenuating circuit. For this sample the 12 pF was a better match to the combined capacitance of the sample and copper plates.

[2]The actual chopper frequency used may vary but it is typically selected to be a frequency that isn't a multiple of 60 Hz.

[3]Mini-Circuits ZASWA-2-50DR+ TTL switch (SPDT)

The fibre laser is set to the frequency of the strongest line based on the data from the laser frequency scan. Above-gap excitation from the 1047 nm laser is used for the previously mentioned reasons. The fibre laser pushes population away from the line it is pumping, resulting in a weak, saturated signal. When the RF comes into resonance with the level splitting of the system it moves population back creating an increase in the photoconductive signal.

3.3.3   Pulsed measurements

For pulsed measurements, the fibre laser, above-gap laser, and RF source are all controlled by the computer. Shutters in the beam paths are used to block the lasers while the RF switch mentioned above is used to turn the RF on and off. Since neither the laser nor the RF are being chopped, the signal must be acquired using a different method.

A measurement begins with initialization of the system by hyperpolarizing it with the pump laser, followed by a dark interval during which RF pulses are applied as detailed in Sec. 2.2. Following this, the pump laser is again turned on from t_0 to t_1 for read out. This time interval is split into two different bins, A and B, as shown in Fig. 3.3.
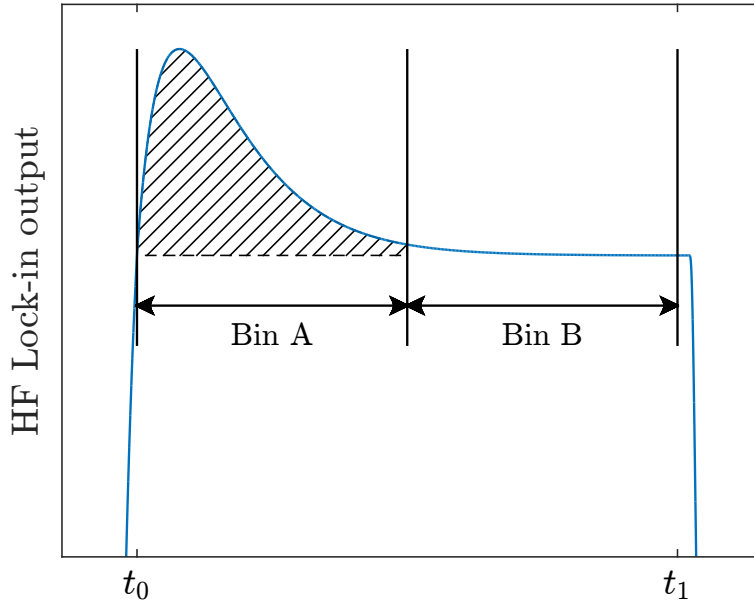

Figure 3.3: Counter A is gated from t_0 to $(t_0+t_1)/2$ while counter B is gated from $(t_0+t_1)/2$ to t_1, where t_0 corresponds to the time when the readout laser is turned on. The number of counts in Bin B is subtracted from the number of counts in Bin A resulting in a signal proportional to the area of the conductivity transient.

To read out the change in population caused by the RF pulses, the photoconductive signal, proportional to change in conductivity, is routed into a voltage-to-frequency converter.

This device generates TTL pulses at a frequency proportional to the signal amplitude. The $V \rightarrow f$ output is connected in parallel to two different counters of a 4-channel gated USB counter. In addition to maintaining backwards compatibility with an older photon counting experiment, the USB counter when connected to the $V \rightarrow f$ allows us to directly record the integrated signal.

One counter is active during interval A and a second counter during interval B, the difference between the two is recorded as the signal and is proportional to the area of the conductivity transient. Both the A and B intervals were typically 75 m sec. Note that the readout cycle acts as the initialization for the following RF cycle.

Specific sequences are programmed into the computer depending on the desired measurement. All sequences are comprised of initialization, manipulation, and readout sections. The manipulation section has one or more precisely timed RF pulses while the readout section has the laser shutters open and the counter triggered. In this experiment, having the laser on during the readout served as the initialization for the next measurement. The different pulse sequences used can be found in Sec. 2.2.

Chapter 4

Results

4.1 Optical scans

The first step of these measurements was to verify the readout method works and the optical spectrum is visible. To that end, multiple laser frequency scans were performed as parameters such as probe laser power, above-gap laser power, and scan speed were adjusted. After optimizing all the parameters, a clean spectrum showing the $F = 0$ and $F = 1$ spectral lines was obtained.

The next step was attempting to hyperpolarize the system. The laser scans were repeated with the addition of a high powered pump laser tuned to either of the lines. Figure 4.1 shows the spectra with no pump laser, the pump laser on $F = 0$, and the pump laser on $F = 1$. From the figure we see that not only is hyperpolarization achievable by pumping either of the lines but that significant population can be moved from one state to the other.

Fitting each spectra to six mixed Gaussian-Lorenztian[1] (three per line) allowed the extraction of the areas of each line as seen in Tab. 4.1. The first thing we noticed is that with no pump laser the ratio of population is $5 : 1$ instead of $3 : 1$ as predicted by the theory. This indicates that the probe laser is saturating the $F = 0$ line despite attempts to avoid this by using very low probe power ($20\,\mathrm{mW}$).

Next we observe that pumping $F = 1$ provides an increase of $\sim 90\%$ in the relative population of the $F = 0$ state whereas pumping $F = 0$ only provides an increase of $\sim 40\%$ to the $F = 1$ population. This and the previous observation can be explained by the fact that when pumping $F = 0$ there are three ways of coming back to $F \neq 0$ compared to only one way of coming back to $F \neq 1$ when pumping $F = 1$. Because of this difference we expect that the $F = 0$ state will be easier to saturate than the $F = 1$ state. This is confirmed by the experimental results.

---

[1] An analytic form for the convolution of a Gaussian with a Lorentzian is not available so an approximation called the Gaussian-Lorentzian Product (GLP) is used.

	No Pump	Pump 1	Pump 0	Theoretical No Laser
Total Area	109	105	136	
$\%_{F=1}$	83%	72%	88%	75%
$\%_{F=0}$	17%	28%	12%	25%
Ratio	5.0 : 1	2.6 : 1	7.0 : 1	3 : 1
Polarization	25%	7%	40%	0%

Table 4.1: **Top:** Hyperpolarization results showing the percentage of total line area for each line under different pump laser configurations. Experimental values are compared to theoretically predicted values. **Bottom:** Polarization values calculated as $\left| 3 \times \%_{F=0} - \%_{F=1} \right| / \left(3 \times \%_{F=0} + \%_{F=1} \right)$.
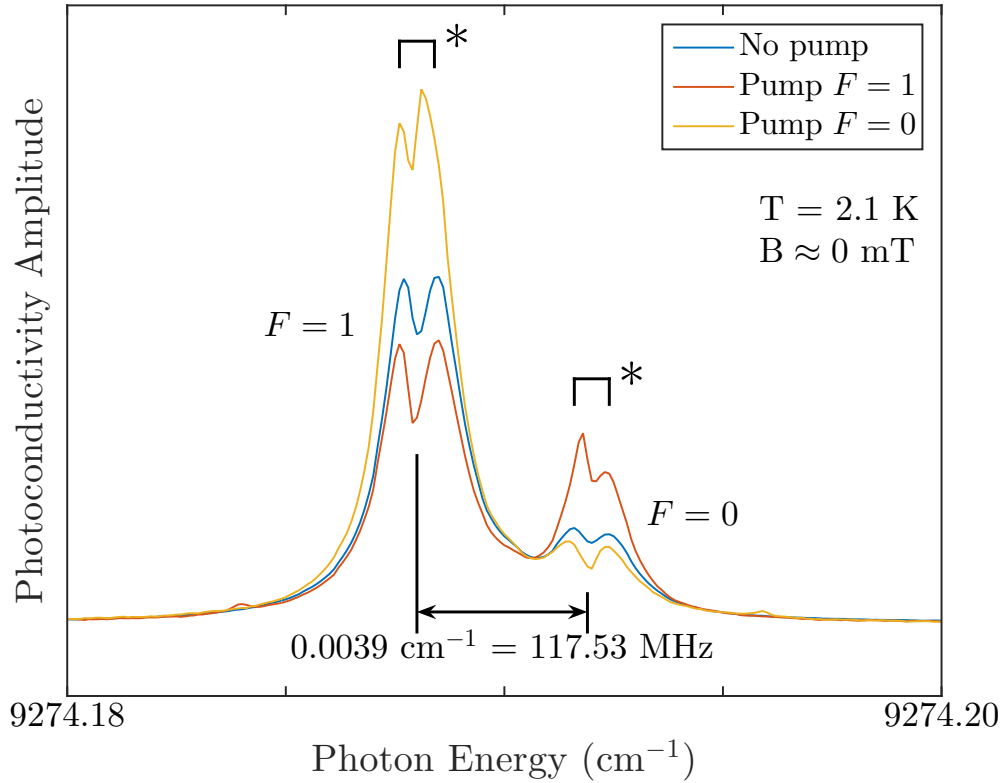

Figure 4.1: "Zero" field optical spectra. Conditions common to all spectra: 20 mW probe, 400 mW pump, 70 μW above-gap excitation. The **blue trace** is with the pump laser turned off, the **orange trace** with the pump laser on the the $F = 1$ line at 9274.188 cm^{-1}, and the **yellow trace** with the pump laser on the $F = 0$ line at 9274.192 cm^{-1}. The asterisks (∗) indicate a splitting of 0.0008 cm^{-1} in each line due to strains present in the sample.

Finally we note the additional splitting of each line into a doublet which is likely due to internal strains present in the sample, which split the hole states of the D^0X but have negligible effect on the D^0 or D^0X electron states. This has been observed before in other measurements of Avogadro material [22]. Fortunately, the magnitude of the splitting (0.0008 cm^{-1}) is small enough that there is not an overlap of the $F = 0$ and $F = 1$ states and we can clearly resolve both of them.

4.2   Magnetic resonance scans

After verifying hyperpolarization was possible, the probe laser was set on the $F = 1$ line and RF was applied to the B_1 coil. The RF frequency was then scanned across the expected transition frequencies and the photoconductive signal was recorded. By measuring the distance between the peaks of the $0 \rightarrow +1$ and $0 \rightarrow -1$ lines, the field was estimated to be $\sim 43\,\mu T$. However, a visual inspection suggested the field was quite inhomogeneous as the $0 \rightarrow \pm 1$ peaks were both broad and asymmetric. Measuring between the inner and outer half-max points of these peaks provided a rough estimate of the lower and upper bounds of the field, $\sim 38\,\mu T$ and $\sim 53\,\mu T$. This was quite problematic as it meant the B_0 field at different parts of the sample differed by close to $\pm 20\%$.

At this point the sample holder was taken apart and measured with a Hall effect sensor. It was determined that the coaxial cable connected to the B_1 coil was magnetic and so it was replaced with a non-magnetic coax. The cryostat was also replaced with a similar unit that had never been used in a magnetic field as measurements using a Hall probe magnetometer indicated that parts of the original cryostat was magnetized. Both active and passive shielding were added to the tail section of the new cryostat as described in Sec. 3.2.1 and the magnetic resonance scans were repeated. The difference in field magnitude before and after was quite substantial as illustrated in Fig. 4.2.

Using the same methods as above, the new field was estimated to be around $4\,\mu T$ before applying any current to the active shielding coils.

At this point the three active shielding coils were connected to three current sources in series with ammeters. Over one hundred scans was performed while adjustments were made to the currents flowing through the $\hat{x}$, $\hat{y}$, and $\hat{z}$ coil-pairs. Initially we aimed to cancel out as much of B_0 as possible and ended up arriving at a field estimated to be less than $0.4\,\mu T$. This can be seen in the bottom-most trace of Fig. 4.3.

Next we separately increased current through the $\hat{x}$ and $\hat{z}$ coils until the measured splitting was approximately equal to $4\,\mu T$. This allowed comparison between the relative population of the $0 \rightarrow \pm 1$ and $0 \rightarrow 0$ lines in the two different B_0 configurations. These results can be seen as the top and middle traces of Fig. 4.3.

The ± 1 transitions appear much stronger when the field is along $\hat{x}$ while the $0 \rightarrow 0$ appears weakened. The strength of the $0 \rightarrow 0$ is basically the same between minimum field
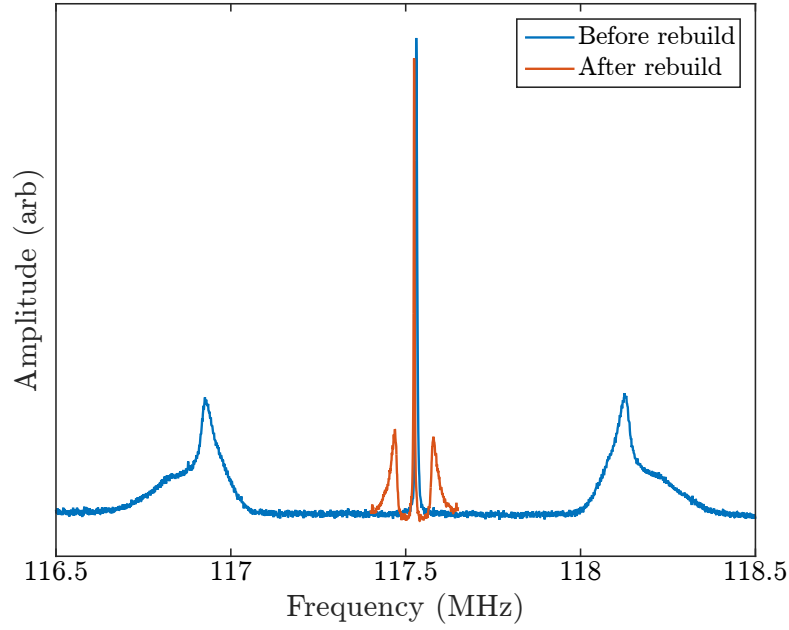
Figure 4.2: Magnetic resonance spectra before and after rebuild. Conditions common to both spectra: T $\approx$ 2.1 K, $\sim$ 30 mW pump/probe laser at 9274.1888 cm^{-1}, and $\sim$ 50 µW above-gap excitation. Blue spectrum was taken with -17 dBm applied to the B_1 coil. Orange spectrum was taken with -10 dBm applied to the B_1 coil.
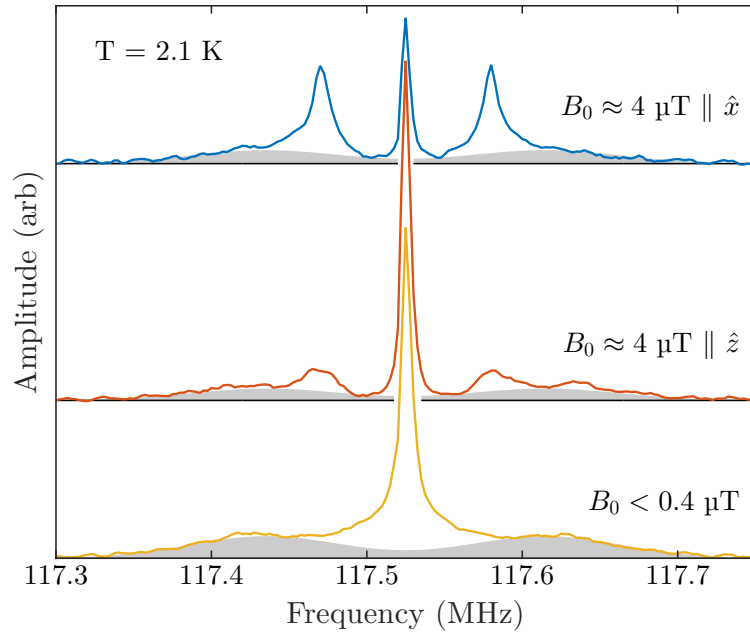

Figure 4.3: Small field magnetic resonance spectra. Conditions common to all spectra: 130 mW pump/probe at 9274.1888 cm^{-1} and 7 µW above-gap excitation. They gray shaded regions are discussed in the text.

and small-$\hat{z}$ field. Also of note are the broad Gaussian areas (in gray) on either side of the $0 \to 0$. Centered at $\sim 117.435\,\text{MHz}$ and $\sim 117.615\,\text{MHz}$ the splitting between them seems to remain constant regardless of the B_0 applied. Calculating the field that would cause such a splitting gives us a $B \approx 6\,\mu\text{T}$. That these broad lines don't move suggests that they are due to internal fields that can't be cancelled out by the external cancellation coils, but which influence only a subset of the donors.

Finally, we used the external coils to apply "large" fields along the $\hat{x}$ and $\hat{z}$ axes. With a few hundred milliamps applied to the coils we were able to create uniform fields of approximately $22\,\mu\text{T}$ and $23\,\mu\text{T}$ along the $\hat{x}$ and $\hat{z}$ axes respectively. The magnetic resonance spectra under these conditions can be seen in Fig. 4.4.
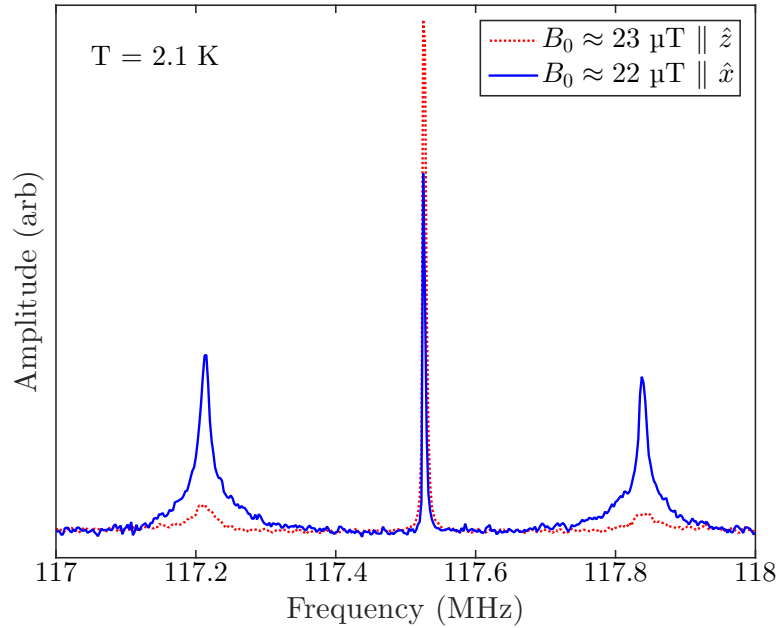

Figure 4.4: Large field magnetic resonance spectra. Conditions common to both spectra: $130\,\text{mW}$ pump/probe at $9274.1888\,\text{cm}^{-1}$ and $7\,\mu\text{W}$ above-gap excitation. Dotted red spectrum was taken with $-17\,\text{dBm}$ applied to the B_1 coil and $198\,\text{mA}$ applied to the B_{0z} coil. Solid blue spectrum was taken with $-10\,\text{dBm}$ applied to the B_1 coil and $285\,\text{mA}$ applied to the B_{0x} coil.

Again we note that the $0 \to \pm 1$ transitions appear stronger when the $B_0 \parallel \hat{x}$, and thus perpendicular to B_1. As expected, the $0 \to 0$ transition is weakened in this configuration since ΔM for this transition is zero and so it should be strongest when $B_0 \parallel B_1$. Looking at the $B_0 \parallel \hat{z}$ we confirm this is the case, here the $0 \to 0$ transition is strongest and the $0 \to \pm 1$ transitions ($\Delta M = \pm 1$) are weakened.

4.3 Pulsed measurements

After performing magnetic resonance scans at each different B_0 configuration we moved onto pulsed measurements. As mentioned in Sec. 2.2, Rabi and Ramsey scans were used to determine the π-pulse length and transition frequency at each field.

Figures 4.5 and 4.6 show Rabi oscillations of $0 \to 0$ and $0 \to \pm 1$ transitions respectively. The difference in SNR is quite apparent. A probable reason for the difference has to do with the frequency composition of the pulses and the width of the different transitions. The shorter the pulse length is in the time domain the broader the pulse is in the frequency domain.

Referring back to Fig. 4.3 we note the widths of the $0 \to 0$ transition versus the widths of the $0 \to \pm 1$ transitions. The $0 \to 0$ has a FWHM $\approx 5\,\mathrm{kHz}$ whereas the $0 \to \pm 1$ has a FWHM of around $20\,\mathrm{kHz}$ for the narrow peak and around $120\,\mathrm{kHz}$ for the broad area. A pulse that is $1\,\mathrm{ms}$ wide in the time domain works out to a pulse that is only about $1\,\mathrm{kHz}$ wide in the frequency domain.

This suggests we were only rotating a fraction of the spins in the $0 \to 0$ transition and an even smaller fraction in the $0 \to \pm 1$ transition. Rotating fewer spins means a smaller signal and therefore a worse SNR. This issue can be worked around by applying more powerful pulses to shorten the required pulse duration.
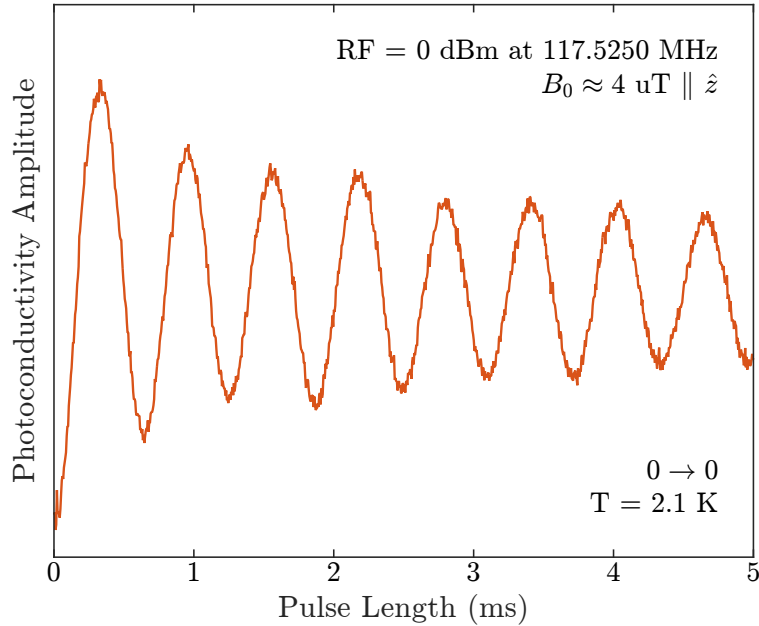

Figure 4.5: Rabi oscillations of the $0 \to 0$ transition with a "small" B_0 field of $4\,\mathrm{\mu T}$ parallel to the $\hat{z}$-axis.
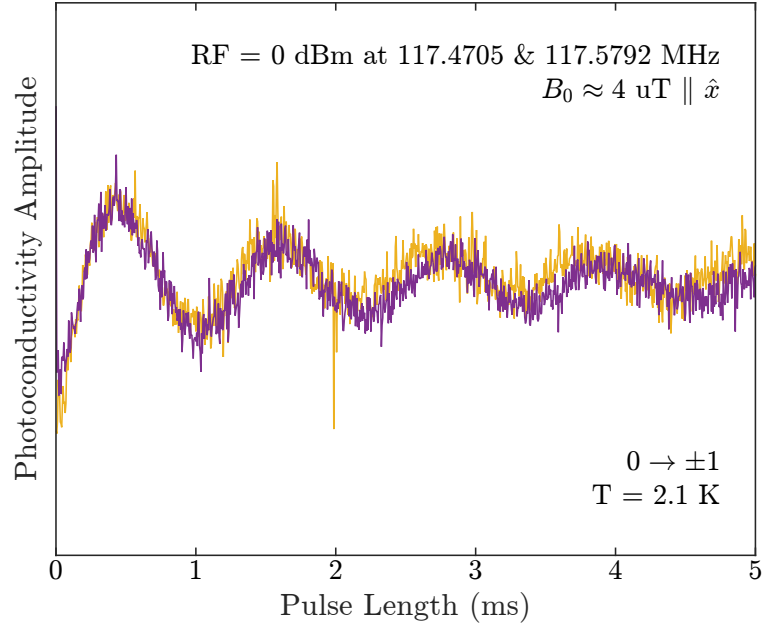
Figure 4.6: Rabi oscillations of the $0 \rightarrow \pm 1$ transition with a "small" B_0 field of $4\,\mu\text{T}$ parallel to the $\hat{x}$-axis. Purple trace is $0 \rightarrow +1$ and orange trace is $0 \rightarrow -1$.
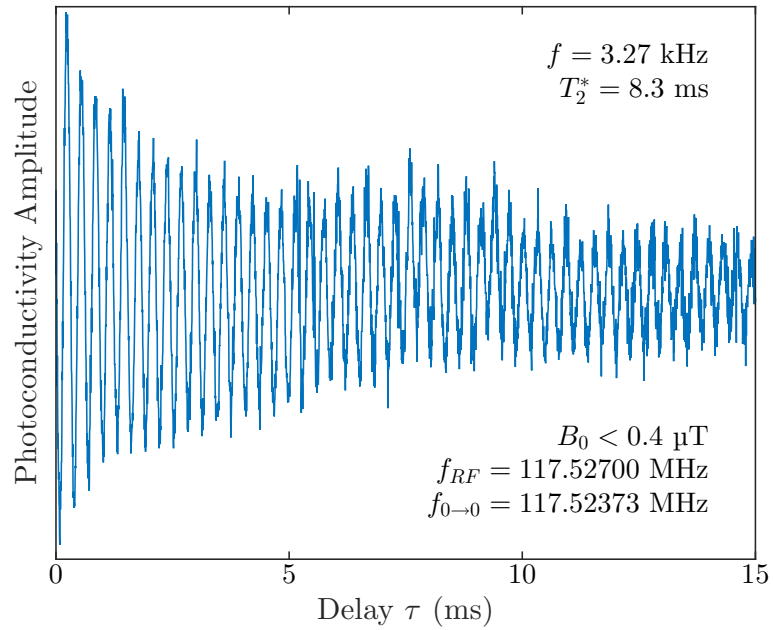

Figure 4.7: "Zero" field Ramsey fringes of the $0 \rightarrow 0$ transition. The pulse sequence consisted of two $70\,\mu\text{s}$ $\pi/2$-pulses of duration with an amplitude of $0\,\text{dBm}$ and frequency, $f_{RF} = 117.527\,\text{MHz}$ separated by a delay, τ.

All Hahn echo decays were fit to the following stretched exponential,

$$a \times \exp\left(-(t/T_2)^n\right), \tag{4.1}$$

where a is an arbitrary amplitude parameter, n the stretching parameter, and T_2 the decay constant. The stretched exponential was used for all fits with n as a parameter after it was observed that some field configurations resulted in decays which could only be fit to a stretched exponential.

First we look at Fig. 4.8, a Hahn echo decay of the $0 \to 0$ transition at the lowest possible field. Transient area is shown versus the delay time, 2τ. The data shown is from a single measurement with no averaging.
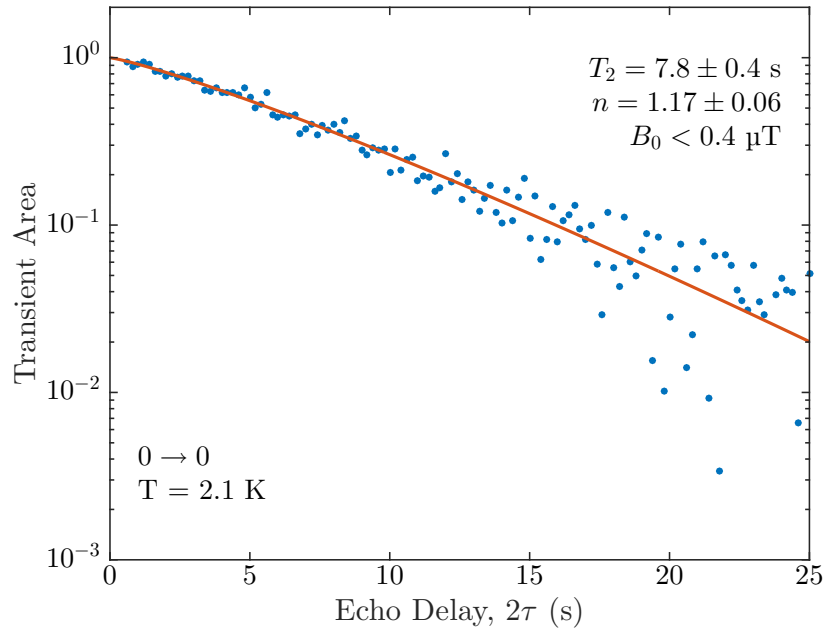

Figure 4.8: Hahn echo data for the $0 \to 0$ transition at the lowest possible field. Laser settings: $130\,\mathrm{mW}$ pump/probe at $9274.1888\,\mathrm{cm}^{-1}$ and $7\,\mu\mathrm{W}$ of above-gap excitation. RF pulse was $0\,\mathrm{dBm}$ at $117.523\,730\,\mathrm{MHz}$.

Fig. 4.9 shows a Hahn echo decay with a small B_0 applied along the $\hat{z}$-axis. Although one would expect that the T_2 should be longest at the lowest field (Fig. 4.8), since zero-field is the perfect clock transition for the $0 \to 0$ transition, we find that this T_2, with a small $B_0 \parallel \hat{z}$, is actually longer.

A possible explanation for this is as follows: at lowest field, population in the $|1, 0\rangle$ state is likely leaking to the $|1, \pm 1\rangle$ states since all three states are nearly degenerate and the T_1 between them should be reduced. This is because as the energy difference between the states approaches zero, the T_1 between the states should also reduce. Once population has

leaked into the $|1, \pm 1\rangle$ states, it would dephase from the $|1, 0\rangle$ since the $|1, 1\rangle$ state would rotate slightly faster, and the $|1, -1\rangle$ state would rotate slightly slower.

This hypothesis is supported by the $n > 1$ stretching parameter which suggests that spectral diffusion is limiting the T_2 decay. Since zero-field is a clock transition for the $0 \to 0$ transition it would have no sensitivity to any magnetic field noise whereas the $0 \to \pm 1$ transitions are not at a clock transition and so they would be sensitive to magnetic field fluctuations.
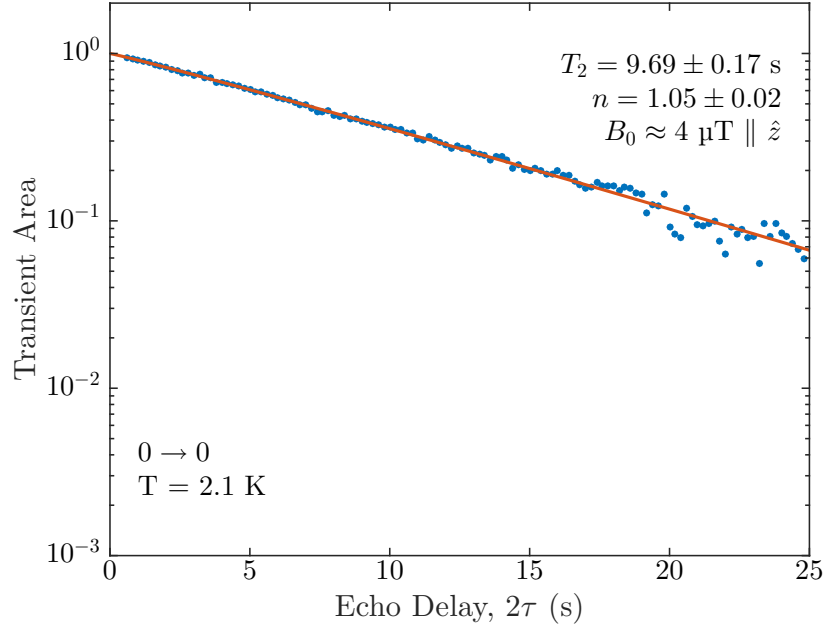

Figure 4.9: Hahn echo data for the $0 \to 0$ transition with a "small" B_0 field of $4\,\mu\text{T}$ parallel to the $\hat{z}$-axis. Laser settings: $130\,\text{mW}$ pump/probe at $9274.1888\,\text{cm}^{-1}$ and $7\,\mu\text{W}$ of above-gap excitation. RF pulse was $0\,\text{dBm}$ at $117.523\,779\,\text{MHz}$.

Figure 4.10 shows the Hahn echo decay of the $0 \to 0$ transition at a field of $23\,\mu\text{T}$ parallel to the $\hat{z}$-axis. This measurement had a particularly low SNR and so it was repeated multiple times. Even so many of the transients had frequent reduced signal glitches which may represent phase noise, a type of amplitude reducing noise caused by a time varying resonance frequency of the donors. This can cause reduced amplitude since the final $\pi/2$-pulse of the Hahn echo won't rotate the spins back to the $\hat{z}$-axis if it is the wrong frequency, since the readout measures the projection of the spins onto the $\hat{z}$-axis this results in seemingly random decreased amplitude glitches.

In order to deal with these glitches, a technique called maximum magnitude detection was used. With this technique, the measurement is repeated multiple times and for each echo delay, the maximum value from all of the repetitions is used. Because the glitches always result in a decrease in amplitude this technique removes the glitches.
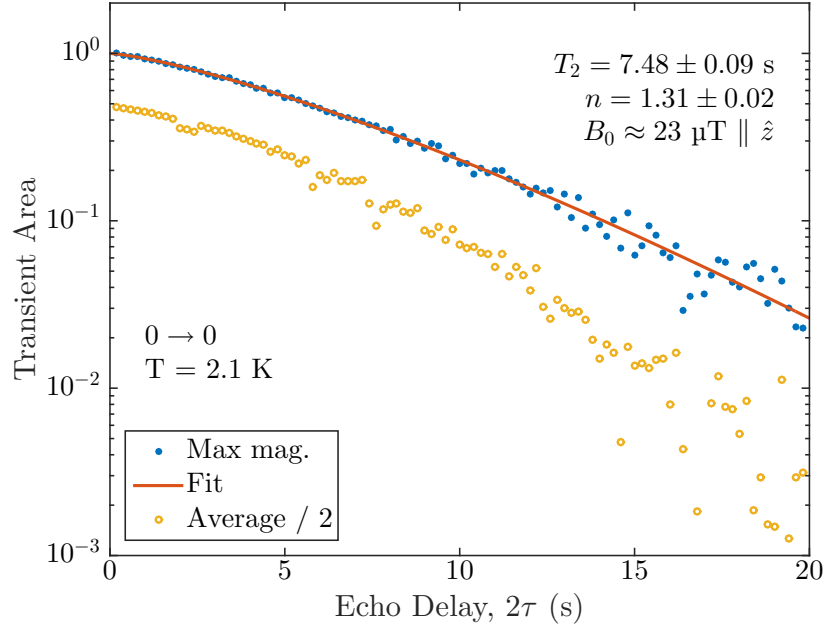
Figure 4.10: Hahn echo data for the $0 \to 0$ transition with a "large" B_0 field of $23\,\mu\text{T}$ parallel to the $\hat{z}$-axis. Laser settings: $130\,\text{mW}$ pump/probe at $9274.1888\,\text{cm}^{-1}$ and $7\,\mu\text{W}$ of above-gap excitation. RF pulse was $33\,\text{dBm}$ at $117.523\,390\,\text{MHz}$.

For comparison, the points calculated by averaging all repetitions are shown underneath the points obtained using the maximum magnitude detection. Ignoring the factor of two used to separate the two datasets, we can clearly see the effect that the zero amplitude glitches have on the average.

Looking at the fit to the maximum magnitude data, we see T_2 at this larger $\hat{z}$-field is decreased from the value we saw for the smaller $\hat{z}$-field and the stretching parameter is the largest observed so far. At this field we are far enough from the clock transition that spectral diffusion related to magnetic field noise starts to affect the T_2.

The final plot, Fig. 4.11, shows the $0 \to \pm 1$ transition with a "large" field applied along the $\hat{x}$-axis ($\perp B_1$). Again we employed maximum magnitude detection to remove the effects of phase noise. Although this field resulted in the strongest possible amplitudes for the $0 \to \pm 1$ transitions of any of the fields used, the T_2 was still not as long as the value measured for the $0 \to 0$ transitions.

The probable explanation for this is that since the $0 \to \pm 1$ are not at a clock transition and therefore have a non-zero $\partial f / \partial B_0$. Any changes in B_0 change the frequency of the transition resulting in a shorter T_2 than for the $0 \to 0$ transition.
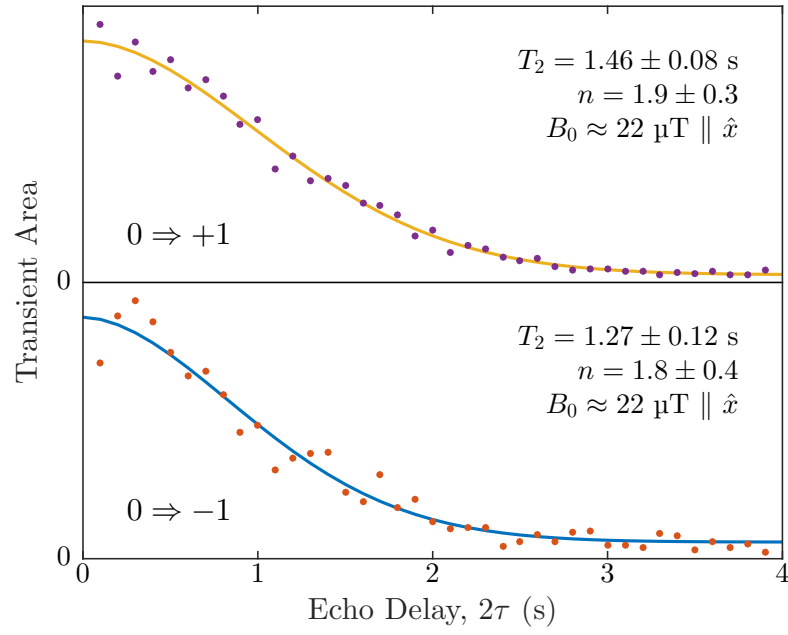
Figure 4.11: Maximum magnitude Hahn echo data for the $0 \rightarrow \pm 1$ transitions with a "large" B_0 field of $22\,\mu\mathrm{T}$ parallel to the $\hat{x}$-axis. Laser settings: $130\,\mathrm{mW}$ pump/probe at $9274.1888\,\mathrm{cm}^{-1}$ and $7\,\mu\mathrm{W}$ of above-gap excitation. RF pulses were $33\,\mathrm{dBm}$ at $117.214\,\mathrm{MHz}$ for the -1 and $117.840\,\mathrm{MHz}$ for the $+1$.

Chapter 5

Conclusion and future direction

In this thesis I demonstrated the ability to manipulate ^{31}P as a qubit in zero field. A sample of isotopically enriched silicon containing the donor phosphorus was studied using continuous-wave optical and magnetic resonance scans as well various pulsed magnetic resonance techniques.

A full set of characterization data was obtained starting with the ability to achieve optical hyperpolarization in this system. Additionally, T_2 measurements showed coherence times of up to ~ 10 s. While not as long as the 39 minute result previously reported by this group, this result required no dynamic decoupling and no large external magnet. Furthermore, 10 s is more than sufficient for use in a future quantum device.

Additionally, many of the techniques and apparatus used for this thesis are currently being used in the study of ^{77}Se [23]. In this case the larger zero field splitting of ~ 1.6 GHz dictates a different approach for applying B_1 as that frequency is outside the range possible for a Helmholtz style coil. Instead we use a split-ring resonator, constructed from copper foil wrapped around a glass tube. The sample is placed in the centre of the tube and the resonator is coupled to using a loop-terminated length of non-magnetic coax cable.

Instead of photo conductive readout, optical absorption is measured by shining a laser through the sample and detecting it using an InAs detector. The InAs detector connected to a current amplifier replaces the entire photo conductive apparatus required by the zero field phosphorus experiments. Optical and magnetic resonance scans still make use of the low frequency lock-in amplifier detecting a chopped signal and pulsed scans still use a counter connected to a voltage-to-frequency converter.

Hyperpolarization measurements used a Bruker FTIR interferometer as a detector while the above mentioned laser was used to pump either the singlet or the triplet state. All other measurements employed just a single laser as both the polarization and readout laser as was done for zero-field phosphorus.

Initial measurements used no magnetic shielding but recently, active $\hat{x}$-, $\hat{y}$-, and $\hat{z}$-coils were used to perform RF and pulsed measurements at various field conditions similar to what was done for phosphorus.

Bibliography

[1] B. E. Kane. A silicon-based nuclear spin quantum computer. *Nature*, 393(6681):133–137, May 1998. `doi:10.1038/30156`.

[2] G Mana, E Massa, CP Sasso, M Stock, K Fujii, N Kuramoto, Shigeki Mizushima, Tomohiro Narukawa, M Borys, I Busch, et al. The correlation of the N_A measurements by counting ^{28}Si atoms. *Journal of Physical and Chemical Reference Data*, 44(3):031209, 2015. `doi:10.1063/1.4921240`.

[3] A Yang, M Steger, D Karaiskaj, M Thewalt, M Cardona, K Itoh, H Riemann, N Abrosimov, M Churbanov, A Gusev, A Bulanov, A Kaliteevskii, O Godisov, P Becker, H J Pohl, J Ager, and E Haller. Optical Detection and Ionization of Donors in Specific Electronic and Nuclear Spin States. *Phys. Rev. Lett.*, 97(22):227401, November 2006. `doi:10.1103/PhysRevLett.97.227401`.

[4] A Yang, M Steger, T Sekiguchi, M Thewalt, T Ladd, K Itoh, H Riemann, N Abrosimov, P Becker, and H J Pohl. Simultaneous Subsecond Hyperpolarization of the Nuclear and Electron Spins of Phosphorus in Silicon by Optical Pumping of Exciton Transitions. *Phys. Rev. Lett.*, 102(25):257401, June 2009. `doi:10.1103/PhysRevLett.102.257401`.

[5] K Saeedi, S Simmons, J Z Salvail, P Dluhy, H Riemann, N V Abrosimov, P Becker, H J Pohl, J J L Morton, and M L W Thewalt. Room-Temperature Quantum Bit Storage Exceeding 39 Minutes Using Ionized Donors in Silicon-28. *Science*, 342(6160):830–833, November 2013. `doi:10.1126/science.1239584`.

[6] Peter Christian Maurer, Georg Kucsko, Christian Latta, Liang Jiang, Norman Ying Yao, Steven D Bennett, Fernando Pastawski, David Hunger, Nicholas Chisholm, Matthew Markham, et al. Room-temperature quantum bit memory exceeding one second. *Science*, 336(6086):1283–1286, 2012. `doi:10.1126/science.1220513`.

[7] Gary Wolfowicz, Alexei M Tyryshkin, Richard E George, Helge Riemann, Nikolai V Abrosimov, Peter Becker, Hans-Joachim Pohl, Mike LW Thewalt, Stephen A Lyon, and John JL Morton. Atomic clock transitions in silicon-based spin qubits. *Nat. Nanotechnol.*, 8(8):561–564, 2013. `doi:10.1038/nnano.2013.117`.

[8] J T Muhonen, A Laucht, S Simmons, J P Dehollain, R Kalra, F E Hudson, S Freer, K M Itoh, D N Jamieson, J C McCallum, A S Dzurak, and A Morello. Quantifying the quantum gate fidelity of single-atom spin qubits in silicon by randomized benchmarking. *J. Phys. Condens. Matter*, 27(15):154205, 2015. `doi:10.1088/0953-8984/27/15/154205`.

[9] Juan P Dehollain, Stephanie Simmons, Juha T Muhonen, Rachpon Kalra, Arne Laucht, Fay Hudson, Kohei M Itoh, David N Jamieson, Jeffrey C McCallum, Andrew S Dzurak, et al. Bell's inequality violation with spins in silicon. *Nat. Nanotechnol.*, 11:242–246, 2015. `doi:10.1038/nnano.2015.262`.

[10] Jeff Z. Salvail, Phillip Dluhy, Kevin J. Morse, Michael Szech, Kamyar Saeedi, Julian Huber, Helge Riemann, Nikolai V. Abrosimov, Peter Becker, Hans-Joachim Pohl, and Michael L. W. Thewalt. Optically enabled magnetic resonance study of ^{75}As and ^{121}Sb in ^{28}Si. *Phys. Rev. B*, 92:195203, Nov 2015. `doi:10.1103/PhysRevB.92.195203`.

[11] Felix Hoehne, Lukas Dreher, Max Suckert, David P. Franke, Martin Stutzmann, and Martin S. Brandt. Time constants of spin-dependent recombination processes. *Phys. Rev. B*, 88:155301, Oct 2013. `doi:10.1103/PhysRevB.88.155301`.

[12] Manuel Cardona and M. L. W. Thewalt. Isotope effects on the optical spectra of semiconductors. *Rev. Mod. Phys.*, 77:1173–1224, Nov 2005. `doi:10.1103/RevModPhys.77.1173`.

[13] R. L. Aggarwal and A. K. Ramdas. Optical determination of the symmetry of the ground states of group-V donors in silicon. *Phys. Rev.*, 140:A1246–A1253, Nov 1965. `doi:10.1103/PhysRev.140.A1246`.

[14] L. Liu. Valence spin-orbit splitting and conduction g tensor in Si. *Phys. Rev. Lett.*, 6:683–685, Jun 1961. `doi:10.1103/PhysRevLett.6.683`.

[15] L. Liu. Effects of spin-orbit coupling in Si and Ge. *Phys. Rev.*, 126:1317–1328, May 1962. `doi:10.1103/PhysRev.126.1317`.

[16] M Steger, T Sekiguchi, A Yang, K Saeedi, M E Hayden, M L W Thewalt, K M Itoh, H Riemann, N V Abrosimov, P Becker, and H J Pohl. Optically-detected NMR of optically-hyperpolarized ^{31}P neutral donors in ^{28}Si. *J. of Appl. Phys.*, 109(10):102411, 2011. `doi:10.1063/1.3577614`.

[17] Gary Wolfowicz, Stephanie Simmons, Alexei M. Tyryshkin, Richard E. George, Helge Riemann, Nikolai V. Abrosimov, Peter Becker, Hans-Joachim Pohl, Stephen A. Lyon, Mike L. W. Thewalt, and John J. L. Morton. Decoherence mechanisms of ^{209}Bi donor electron spins in isotopically pure ^{28}Si. *Phys. Rev. B*, 86:245301, Dec 2012. `doi:10.1103/PhysRevB.86.245301`.

[18] W. Schmid. Auger lifetimes for excitons bound to neutral donors and acceptors in si. *Physica Status Solidi (B)*, 84(2):529–540, 1977. `doi:10.1002/pssb.2220840216`.

[19] P Becker, H J Pohl, H Riemann, and N Abrosimov. Enrichment of silicon for a better kilogram. *Phys. Status Solidi A*, 207(1):49–66, January 2010. `doi:10.1002/pssa.200925148`.

[20] P. McL. Colley and E. C. Lightowlers. Calibration of the photoluminescence technique for measuring B, P and Al concentrations in Si in the range 10^{12} to 10^{15} cm^{-3} using Fourier transform spectroscopy. *Semiconductor Science and Technology*, 2(3):157, 1987. `doi:10.1088/0268-1242/2/3/005`.

[21] Albion Yang. *Optical hyperpolarization and detection of electron and nuclear spins of phosphorus donors in highly enriched ^{28}Si.* PhD thesis, Simon Fraser University, 2012.

[22] M. L. W. Thewalt, A. Yang, M. Steger, D. Karaiskaj, M. Cardona, H. Riemann, N. V. Abrosimov, A. V. Gusev, A. D. Bulanov, I. D. Kovalev, A. K. Kaliteevskii, O. N. Godisov, P. Becker, H. J. Pohl, E. E. Haller, J. W. Ager, and K. M. Itoh. Direct observation of the donor nuclear spin in a near-gap bound exciton transition: ^{31}P in highly enriched ^{28}Si. *Journal of Applied Physics*, 101(8):081724, 2007. `doi: 10.1063/1.2723181`.

[23] Kevin J. Morse, Rohan J. S. Abraham, Helge Riemann, Nikolai V. Abrosimov, Peter Becker, Hans-Joachim Pohl, Michael L. W. Thewalt, and Stephanie Simmons. A photonic platform for donor spin qubits in silicon, 2016. `arXiv:1606.03488`.
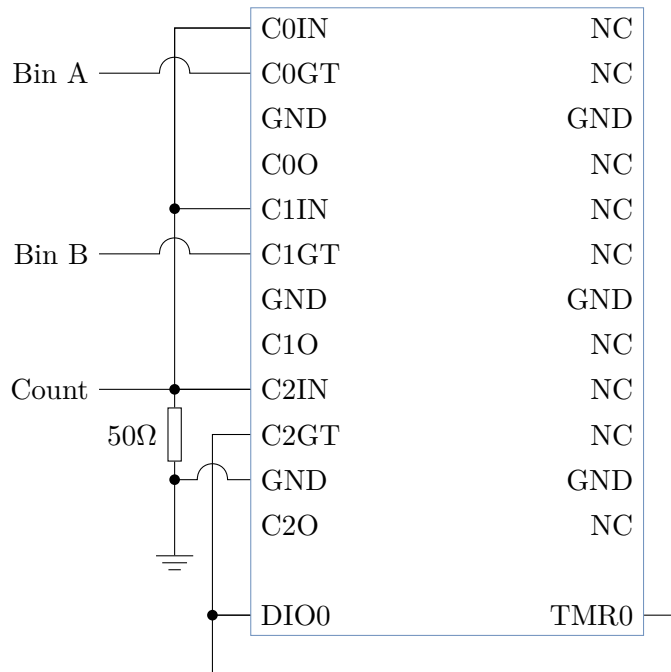
Appendix A

Diagrams

Figure A.1: Wiring diagram for the Measurement Computing USB-CTR04 used to count pulses from the voltage-to-frequency converter. When carrying out pulsed measurements Counters 0 and 1 are gated by external TTL signals from a SpinCore PulseBlaster. When carrying out optical scans, Timer 0 is used to gate Counter 2 for the desired measurement interval and DIO 0 is used as a software polled input to determine when the measurement has completed.
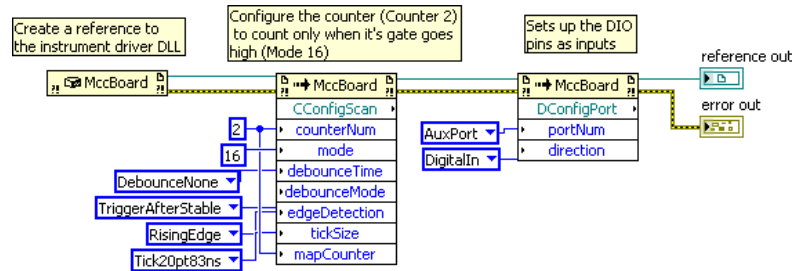
Appendix B

Code

Figure B.1: When performing optical scans Counter 2 is setup to count the pulses from the voltage-to-frequency converter and `AuxPort` (DIO 0) is configured as `DigitalIn` so it can be used to read the gate level.
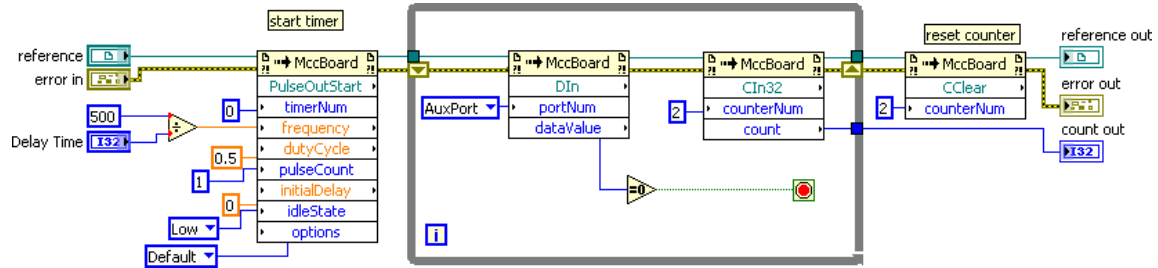

Figure B.2: Timer 0 is used to gate Counter 2 when performing optical scans. This allows for accurate and precise measurement intervals. Due to a missing feature in the counter driver there is no way to determine the gate level using software. For this reason the level of `AuxPort` (DIO 0) is polled by LabVIEW to determine when the measurement interval is complete.
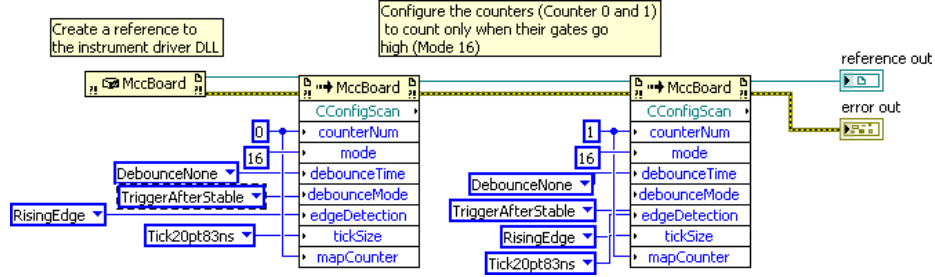
Figure B.3: When performing optical scans Counters 0 and 1 are setup to count the pulses from the voltage-to-frequency converter. Counters 0 and 1 are both gated externally by the PulseBlaster.
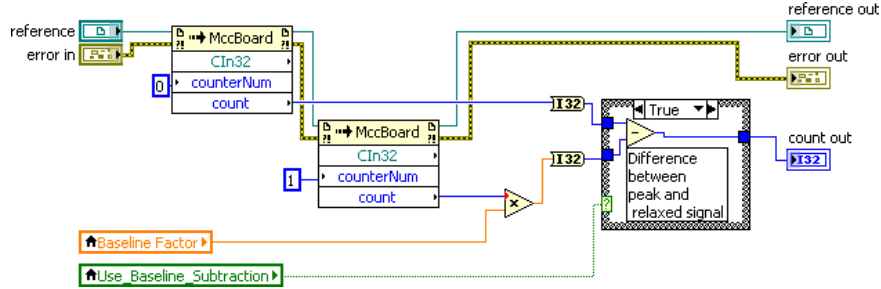

Figure B.4: The number of counts from Counter 1 is multiplied by `Baseline Factor` and subtracted from the number of counts from Counter 0. `Baseline Factor` is used to scale the counts in the situation where Bin A and Bin B are different lengths.